TEMPLATE MATCHING ON VECTOR FIELDS USING CLIFFORD ALGEBRA

J. Ebling, and G. Scheuermann

FB Informatik, University of Leipzig
04315 Leipzig, Germany.
E-mail:{ebling,scheuer}@informatik.uni-leipzig.de

Keywords: Flow visualization, template matching, Clifford algebra, Fourier transform

Abstract.   *Due to the amount of flow simulation and measurement data, automatic detection, classification and visualization of features is necessary for an inspection. Therefore, many automated feature detection methods have been developed in recent years. However, one feature class is visualized afterwards in most cases, and many algorithms have problems in the presence of noise or superposition effects. In contrast, image processing and computer vision have robust methods for feature extraction and computation of derivatives of scalar fields. Furthermore, interpolation and other filter can be analyzed in detail. An application of these methods to vector fields would provide a solid theoretical basis for feature extraction. The authors suggest Clifford algebra as a mathematical framework for this task.*

Clifford algebra provides a unified notation for scalars and vectors as well as a multiplication of all basis elements. The Clifford product of two vectors provides the complete geometric information of the relative positions of these vectors. Integration of this product results in Clifford correlation and convolution which can be used for template matching on vector fields. Furthermore, for frequency analysis of vector fields and the behavior of vector-valued filters, a Clifford Fourier transform has been derived for 2 and 3 dimensions. Convolution and other theorems have been proved, and fast algorithms for the computation of the Clifford Fourier transform exist. Therefore the computation of Clifford convolution can be accelerated by computing it in Clifford Fourier domain. Clifford convolution and Fourier transform can be used for a thorough analysis and subsequent visualization of vector fields.

1

1 INTRODUCTION

Visualization and analysis of vector fields from flow simulations and measurements is an important step in engineering processes, e.g. during the design phase of airplanes, cars, trains, and combustion chambers. A specific role in these visualizations play features, which are often defined as "phenomena, structures or objects in a data set, that are of interest for a certain research or engineering problem" [19]. It is not possible to give a list of all features of interest in a flow field as these differ from application to application and small changes of one feature lead to a variety of new features. Nevertheless, most features can be categorized into a few groups like vortices and other swirling flows, shock waves, shear flow and boundary layers, reversed flow, saddle points, separation and attachment lines or surfaces, areas with convergent or divergent behavior, and regions with homogeneous or constant flow.

Most flow simulations and measurements want to study overall structure and specific features, i.e. patterns of streamlines with conspicuous behavior. Flow visualization intends to help the user to find and analyze features and structures. Direct visualization methods like hedgehogs do not always reveal the features. Streamline based methods may lead to missing features, too, especially without knowing the right starting points. Texture based methods like line integral convolution [5] do a quite good job in 2D, but a convincing solution in 3D is still missing. Topology [15,6,24,23,27,28,26], on the other hand, is directed to the overall structure since not all features are easily connected to it. Furthermore, the presentation of 3D topology produces visibility problems. Another, quite different, approach for the visualization is to use information visualization methods like brushing for interactive exploration of the data sets [7].

A huge amount of data is generated nowadays by flow simulations and measurements. The resulting vector fields often contain millions of data values, but even for small datasets with only thousands of values, direct inspection by the user is tedious and features are missed easily. Therefore, many automated feature detection methods have been developed in recent years (e.g. [8, 14, 18, 25, 22, 19]. Streamlines can be used in a second step to study the features. Earlier attempts usually try to give an analytic model of a feature and create an algorithm for feature detection from there. Besides the limitations of the models, most approaches have severe robustness problems.

Image processing and computer vision are mature fields and have produced methods for analysis, feature extraction and derivative computation [16, 17]. Convolution based approaches are robust in terms of white noise because of the inherent averaging present in the convolution method. Furthermore, many image processing methods allow precise analysis of accuracy for operations including sampling, interpolation and smoothing. Noise is also suitably modeled and dealt with. Therefore, it is be sensible to apply these methods to vector fields. The convolution operation has already been extended to vector fields which has lead to the creation of pattern matching algorithms for vector fields.

One of the difficulties of applying, for example, correlation based methods to vector fields lies in the definition of a suitable multiplication of vectors. Clifford algebra can resolve this problem as a unified multiplication of scalar, vectors and general elements of this algebra (called multivectors) does exist. By using this algebra, Clifford convolution and a corresponding Fourier transform for 2D and 3D can be defined [8,9].

The depth and precision of flow field analysis based on template matching and Clifford convolution is studied in detail for two different applications. The first application are flow fields measured in the wake of a helicopter rotor [3,4,20,29,11]. Determining the features and their parameters in this data is an important step for a better understanding of the observed flow.

Specific techniques dealing with subpixel accuracy and the parameters to be determined are developed on the way. To regard the flow as a superposition of simpler features is a necessity for this application as close vortices influence each other. Convolution is a linear system, so it is suited for this kind of analysis. The next application is a gas furnace chamber. The flow in this chamber is quite turbulent due do the desired mixing of air and gas. Based on Clifford correlation, a feature based segmentation of the flow is computed and visualized [10]. The resulting visualization displays important structures of the flow and highlights the interesting features.

In Section 2, related work on template matching and Fourier transforms of vector valued is discussed. An introduction to Clifford algebra is given in Section 3 and the Clifford convolution is described in Section 4. In Section 5, the Clifford Fourier transform is defined along with the theorems. Examples of Clifford convolution and Clifford Fourier transform are given in Section 6. Analysis and visualization of vector fields using template matching is described for two different applications in Section 7, and the conclusion can be found in Section 8.

2 RELATED WORK

An obvious approach to image processing of vector fields is to decompose the field into its components for subsequent independent processing using known tools such as convolution and the Fourier transform. Granlund and Knutsson [13] have investigated this approach in 2D. However, a vector represents more information than its separated components. The scalar fields of the components are not independent and do not provide insight into the vector as a whole.

Another definition of the convolution is the generalized inner product of pertinent vectors. Heiberg et al. [14] define convolution on vector fields using the inner (or scalar) product of two vectors as

$$(\mathbf{h} *_s \mathbf{f})(\mathbf{x}) := \int_{E^d} \langle \mathbf{h}(\mathbf{x'}), \mathbf{f}(\mathbf{x} - \mathbf{x'}) \rangle d\mathbf{x'}, \tag{1}$$

where $\mathbf{f}$ is the normalized vector field and $\mathbf{h}$ is the filter. The scalar product provides an approximation to the cosine of the angle between the direction of patterns present in the vector field and the direction of the filter. Heiberg et al. do not formulate or use a Fourier transform in their method.

Extensions of the Fourier transform to vector fields arose from a different area of research, namely texture segmentation. In 1D, an analytic signal is used to analyze the local phase and amplitude. The analytic signal consists of a signal and its Hilbert transform and is zero for all negative frequencies. While giving extensions of the analytic signal to 2D, Bülow [2] and Felsberg [12] defined some Fourier transforms within Clifford algebra.

Bülow [2] used a Clifford algebra where $\mathbf{e}_j^2 = -1$ and defined the d-dimensional Fourier transform by using the bases $\{\mathbf{e}_1, ..., \mathbf{e}_d\}$ in the Fourier kernel as

$$\mathscr{F}_b\{\mathbf{f}\}(\mathbf{u}) := \int_{E^d} \mathbf{f}(\mathbf{x}) \prod_{k=1}^{d} e^{(-\mathbf{e}_k 2\pi x_k u_k)} |d\mathbf{x}|. \tag{2}$$

(The product has to be performed in the fixed order of the indices.) The corresponding convolution theorems are rather complicated. The complex form of the kernel and the non-commutativity of the multiplication present a problem when trying to establish a fast version of this Fourier transform.

3

Felsberg [12] extended the analytic signal in 1D to the monogenic signal in 2D by using embedded functions to obtain additional phases. Therefore, he composed vectors by combining spatial coordinates and a corresponding function value, $v(x_1, x_2) = (x_1, x_2, f(x_1, x_2))$. He defined his Fourier transform for arbitrary multivector-valued functions $\mathbf{F} \in G_2$ (in 1D) and $\mathbf{F} \in G_3$ (in 2D) as

$$\mathscr{F}\{\mathbf{F}\}(\mathbf{u}) := \int_{x_1} e^{(-2\pi i_2 \langle \mathbf{x}, \mathbf{u} \rangle)} \mathbf{F}(\mathbf{x}) dx_1 \tag{3}$$

with $\mathbf{x} = x\mathbf{e}_1$ in 1D and

$$\mathscr{F}\{\mathbf{F}\}(\mathbf{u}) := \int_{x_1} \int_{x_2} e^{(-2\pi i_3 \langle \mathbf{x}, \mathbf{u} \rangle)} \mathbf{F}(\mathbf{x}) dx_1 dx_2 \tag{4}$$

with $\mathbf{x} = x_1\mathbf{e}_1 + x_2\mathbf{e}_2$ in 2D. The values i_2 and i_3, which are interpreted as complex numbers, are defined in Section 3. Felsberg defined the convolution only for quaternion (in 1D) and spinor (in 2D) valued filters on vector-valued functions [12], thus, no vector-valued filter for pattern matching on vector fields could be applied. As the convolution was restricted, so was the convolution theorem. Concerning other theorems like derivative and Parseval's theorem, only special cases of the multivector-valued functions were considered. We extend this approach by using Clifford convolution and proving theorems for arbitrary multivector-valued functions.

Another definition of a Fourier transform within Clifford algebra comes from mathematical theory. Brackx et al. [1] pursue the idea of refining the Fourier transform by using operator notation and defining a pair of transformations whose harmonic average is the classical Fourier transform. They also use a Clifford algebra where the square of the unit-vectors is $\mathbf{e}_j^2 = -1$.

3 CLIFFORD ALGEBRA

Definition 3.1 *For the n-dimensional Euclidean vector space E^n with basis $\{e_1, .., e_n\}$, the 2^n-dimensional* **Clifford** *or* **geometric algebra** *G_n is defined as a direct sum $V_0 \oplus V_1 \oplus ... \oplus V_n$ with the basis elements from the following table*

space	name	grad	dimension	basiselements
V_0	*scalars*	0	$\binom{n}{0} = 1$	1
V_1	*vectors*	1	$\binom{n}{1} = n$	$e_1, .., e_n$
V_2	*bivectors*	2	$\binom{n}{2}$	$e_j e_k, j < k$
V_3	*trivectors*	3	$\binom{n}{3}$	$e_j e_k e_l, j < k < l$
$\vdots$	$\vdots$	$\vdots$	$\vdots$	$\vdots$
V_k	$k - vectors$	k	$\binom{n}{k}$	$e_{j_1} e_{j_2} ... e_{j_k}, j_1 < ... < j_k \in 1, .., n$
$\vdots$	$\vdots$	$\vdots$	$\vdots$	$\vdots$
V_n	$n - vectors$	n	$\binom{n}{n} = 1$	$e_1 .. e_n = i_n$

together with the associative, bilinear **geometric product**

$$G_n \times G_n \to G_n,$$
$$(A, B) \mapsto AB \tag{5}$$

given by

$$
\begin{array}{rcll}
1e_j &=& e_j, & j \in \{1, .., n\}\,, \\
e_j e_j &=& 1, & j \in \{1, .., n\}\,, \\
and \quad e_j e_k &=& -e_k e_j, & j, k \in \{1, .., n\}, j \neq k\,.
\end{array} \tag{6}
$$

Definition 3.2 *An arbitrary element of G_n is called* **multivector***. An element $A \in V_k$ which can be written as $A = \alpha e_{j_1} e_{j_2} ... e_{j_k}$, $\alpha \in \mathbb{R}$ is called* **k-blade***.*

In G_n, the n-blade $\mathbf{e}_1..\mathbf{e}_n$ is also called pseudoscalar. It is denoted by $\boldsymbol{i}$, or $\boldsymbol{i}_n$ when indicating that the pseudoscalar of G_n is meant.

Definition 3.3 *The canonic projection $\langle \cdot \rangle_k : G_n \to G_n, A \mapsto \langle A \rangle_k$ is called* **k-projector***.*

Definition 3.4 *The* **dual** *of a multivector A is defined as $\boldsymbol{i}A$.*

Thus, the dual of a r-blade is a (n-r)-blade. Clifford multiplication of two vectors $\mathbf{a}, \mathbf{b} \in E^n$ results in

$$\mathbf{ab} = \langle \mathbf{a}, \mathbf{b} \rangle + \mathbf{a} \wedge \mathbf{b}, \tag{7}$$

where $\langle , \rangle$ is the inner product and $\wedge$ is the outer product. In 2D and 3D, this results in

$$
\begin{aligned}
\langle \mathbf{ab} \rangle_0 &= \langle \mathbf{a}, \mathbf{b} \rangle = \|\mathbf{a}\| \, \|\mathbf{b}\| \cos \omega \\
and \quad \|\langle \mathbf{ab} \rangle_2\| &= \|\mathbf{a} \wedge \mathbf{b}\| = \|\mathbf{a}\| \, \|\mathbf{b}\| \sin \omega,
\end{aligned} \tag{8}
$$

where ω is the angle between $\mathbf{a}$ and $\mathbf{b}$ and $\langle \mathbf{ab} \rangle_2$ corresponds to the plane through $\mathbf{a}$ and $\mathbf{b}$ — the corresponding bivector.

Definition 3.5 *The* **Riemann integral** *of a multivector-valued function $\boldsymbol{F}$ is defined as*

$$\int_{E^n} \boldsymbol{F}(x) |dx| := \lim_{\substack{|\Delta x_j| \to 0 \\ k \to \infty}} \sum_{i=1}^{k} \boldsymbol{F}(x_j e_j) |\Delta x_j| \,. \tag{9}$$

The quantity $|d\mathbf{x}|$ is used to make the integral grade preserving since $d\mathbf{x}$ is a vector within Clifford algebra.

Definition 3.6 *The* **directional derivative** *of $\boldsymbol{F}$ in direction $\mathbf{r}$ is*

$$\boldsymbol{F}_{\boldsymbol{r}}(x) := \lim_{h \to 0} \frac{[\boldsymbol{F}(x + h\boldsymbol{r}) - \boldsymbol{F}(x)]}{h} \tag{10}$$

with $h \in \mathbb{R}$.

Definition 3.7 *The* **vector derivative** ∇ *is defined as*

$$\nabla := \sum_{j=1}^{n} e_j \frac{\partial}{\partial x_j} \tag{11}$$

Note that ∇ is vector valued, and computation of the derivative can now be done using the geometric product:

Definition 3.8 *The (complete)* **derivative** *of F from the left is*

$$\nabla F(\boldsymbol{x}) := \sum_{j=1}^{n} \boldsymbol{e}_j F\boldsymbol{e}_j(\boldsymbol{x}), \tag{12}$$

where $F\boldsymbol{e}_j(\boldsymbol{x})$ are the directional derivatives. The derivative from the right is

$$F(\boldsymbol{x})\nabla := \sum_{j=1}^{n} F\boldsymbol{e}_j(\boldsymbol{x})\boldsymbol{e}_j . \tag{13}$$

Definition 3.9 Curl *and* **divergence** *of a 2D or 3D vector-valued function f are defined as*

$$\begin{aligned} curl\,\boldsymbol{f} &:= \nabla \wedge \boldsymbol{f} = \frac{(\nabla \boldsymbol{f} - \boldsymbol{f}\nabla)}{2} \\ and \quad div\,\boldsymbol{f} &:= \langle \nabla, \boldsymbol{f} \rangle = \frac{(\nabla \boldsymbol{f} + \boldsymbol{f}\nabla)}{2}. \end{aligned} \tag{14}$$

This curl operator gives the bivector describing the plane of strongest rotation whereas the classical curl operator results in the corresponding normal vector. As $(\boldsymbol{i}_2)^2 = -1$ and $(\boldsymbol{i}_3)^2 = -1$,

$$\{\alpha + \boldsymbol{i}_2\beta \,|\, \alpha, \beta \in \mathbb{R}\} \subset G_2 \tag{15}$$

and

$$\{\alpha + \boldsymbol{i}_3\beta \,|\, \alpha, \beta \in \mathbb{R}\} \subset G_3 \tag{16}$$

are isomorphic to the complex numbers $\mathbb{C}$.

4 CLIFFORD CONVOLUTION

Definition 4.1 *Let $f_1, f_2 : \mathbb{R} \to C$ be continuous signals and let $t, k \in \mathbb{R}$.* **Convolution** *of f_1 and f_2 is defined as*

$$(f_1 * f_2)(t) := \int_{\mathbb{R}} f_1(k)f_2(t-k)dk. \tag{17}$$

Spatial **correlation** *of f_1 and f_2 is defined as*

$$(f_1 \star f_2)(t) := \int_{\mathbb{R}} f_1(k)f_2(t+k)dk. \tag{18}$$

Definition 4.2 *Let F be a multivector-valued field and H a multivector-valued filter. Then* **Clifford convolution** *based on the geometric product is defined as*

$$(H *_l F)(\boldsymbol{x}) := \int_{\mathbb{R}^n} H(\boldsymbol{x'})F(\boldsymbol{x}-\boldsymbol{x'})|d\boldsymbol{x'}| \tag{19}$$

and analog

$$(F *_r H)(\boldsymbol{x}) := \int_{\mathbb{R}^n} F(\boldsymbol{x}-\boldsymbol{x'})H(\boldsymbol{x'})|d\boldsymbol{x'}| \tag{20}$$

Definition 4.3 *Let F be a multivector-valued field and H a multivector-valued filter. Then* **Clifford correlation** *based on the geometric product is defined as*

$$(H \star_l F)(x) := \int_{\mathbb{R}^n} H(x')F(x+x')|dx'| \tag{21}$$

and analog

$$(F \star_r H)(x) := \int_{\mathbb{R}^n} F(x+x')H(x')|dx'| \tag{22}$$

Clifford convolution is, therefore, an extension of the convolution on scalar fields. However, it is also an extension of the scalar convolution defined by Heiberg et al. [14] since

$$(\mathbf{h} *_s \mathbf{f})(\mathbf{x}) := \int_{E^d} \langle \mathbf{h}(\mathbf{x'}), \mathbf{f}(\mathbf{x} - \mathbf{x'}) \rangle d\mathbf{x'} \tag{23}$$

provides

$$(\mathbf{h} *_s \mathbf{f})(\mathbf{x}) = \langle (\mathbf{h} *_l \mathbf{f}) \rangle_0 = \langle (\mathbf{f} *_r \mathbf{h}) \rangle_0 \tag{24}$$

for vector fields $\mathbf{h}, \mathbf{f}$.

5 CLIFFORD FOURIER TRANSFORM

5.1 Fourier Transform on Scalar Fields

For continuous signals $f, h : E^d \to C$, the Fourier transform of f is defined as

$$\mathscr{F}\{f\}(\mathbf{u}) := \int_{E^d} f(\mathbf{x}) e^{(-2\pi i \langle \mathbf{x}, \mathbf{u} \rangle)} d\mathbf{x} \tag{25}$$

with $i^2 = -1$ provided the integral exists. The inverse transform is defined as

$$\mathscr{F}^{-1}\{f\}(\mathbf{u}) := \int_{E^d} f(\mathbf{x}) e^{(2\pi i \langle \mathbf{x}, \mathbf{u} \rangle)} d\mathbf{x} . \tag{26}$$

The convolution theorem is

$$\mathscr{F}\{h * f\}(\mathbf{u}) = \mathscr{F}\{h\}(\mathbf{u})\mathscr{F}\{f\}(\mathbf{u}) \tag{27}$$

and the derivative theorems are

$$\mathscr{F}(\nabla f)(\mathbf{x}) = 2\pi i \mathbf{u} \mathscr{F}\{f\}(\mathbf{u}) \text{ and} \tag{28}$$

$$\mathscr{F}(\Delta f)(\mathbf{x}) = -4\pi^2 \mathbf{u}^2 \mathscr{F}\{f\}(\mathbf{u}). \tag{29}$$

5.2 Clifford Fourier Transform in 3D

Definition 5.1 *Let $F : \mathbb{R}^3 \to G_3$ be a multivector-valued signal. Let $x, u \in \mathbb{R}^3$. The* **Clifford Fourier transform** *(CFT) of F is defined as*

$$\mathscr{F}\{F\}(u) := \int_{\mathbb{R}^3} F(x) e^{(-2\pi i_3 \langle x, u \rangle)} |dx|. \tag{30}$$

The inverse transformation is then given by

$$\mathscr{F}^{-1}\{F\}(x) := \int_{\mathbb{R}^3} F(u) e^{(2\pi i_3 \langle x, u \rangle)} |du|. \tag{31}$$

Note that the Clifford Fourier kernel $e^{(-2\pi i_3\langle \mathbf{x}, \mathbf{u}\rangle)}$ is multivector valued. To be more exact, it consists of a scalar and a pseudoscalar.

Lemma 5.2 *For every scalar γ, we have*

$$e^{(i_3\gamma)} = cos(\gamma) + i_3 sin(\gamma) \tag{32}$$

and for every multivector $A \in G_3$

$$Ae^{(i_3\gamma)} = e^{(i_3\gamma)}A. \tag{33}$$

Proof:

$$
\begin{aligned}
Ae^{(i_3\gamma)} &= A cos(\gamma) + A i_3 sin(\gamma) \\
&= cos(\gamma)A + i_3 sin(\gamma)A \\
&= e^{(i_3\gamma)}A\ .
\end{aligned}
\tag{34}
$$

Theorem 5.3 *The Clifford Fourier transform is a linear combination of four classical Fourier transforms.*
Proof: *For a multivector field $\mathbf{F} : \mathbb{R}^3 \to G_3$, we have*

$$
\begin{aligned}
\mathbf{F}(\mathbf{x}) &= \mathbf{F}_0(\mathbf{x}) + \mathbf{F}_1(\mathbf{x})\mathbf{e}_1 + \mathbf{F}_2(\mathbf{x})\mathbf{e}_2 + \mathbf{F}_3(\mathbf{x})\mathbf{e}_3 \\
&+ \mathbf{F}_{23}(\mathbf{x})\mathbf{e}_{23} + \mathbf{F}_{31}(\mathbf{x})\mathbf{e}_{31} + \mathbf{F}_{12}(\mathbf{x})\mathbf{e}_{12} + \mathbf{F}_{123}(\mathbf{x})\mathbf{e}_{123} \\
&= \mathbf{F}_0(\mathbf{x}) + \mathbf{F}_1(\mathbf{x})\mathbf{e}_1 + \mathbf{F}_2(\mathbf{x})\mathbf{e}_2 + \mathbf{F}_3(\mathbf{x})\mathbf{e}_3 \\
&+ \mathbf{F}_{23}(\mathbf{x})i_3\mathbf{e}_1 + \mathbf{F}_{31}(\mathbf{x})i_3\mathbf{e}_2 + \mathbf{F}_{12}(\mathbf{x})i_3\mathbf{e}_3 + \mathbf{F}_{123}(\mathbf{x})i_3
\end{aligned}
\tag{35}
$$

which can be regarded as four complex signals:

$$
\begin{aligned}
\mathbf{F}(\mathbf{x}) &= [\mathbf{F}_0(\mathbf{x}) + \mathbf{F}_{123}(\mathbf{x})i_3]1 \\
&+ [\mathbf{F}_1(\mathbf{x}) + \mathbf{F}_{23}(\mathbf{x})i_3]\mathbf{e}_1 \\
&+ [\mathbf{F}_2(\mathbf{x}) + \mathbf{F}_{31}(\mathbf{x})i_3]\mathbf{e}_2 \\
&+ [\mathbf{F}_3(\mathbf{x}) + \mathbf{F}_{12}(\mathbf{x})i_3]\mathbf{e}_3
\end{aligned}
\tag{36}
$$

This can be interpreted as an element of $\mathbb{C}^4$. Considering the linearity of the Clifford Fourier transform, we get

$$
\begin{aligned}
\mathscr{F}\{\mathbf{F}\}(\mathbf{u}) &= [\mathscr{F}\{\mathbf{F}_0(\mathbf{x}) + \mathbf{F}_{123}(\mathbf{x})i_3\}(\mathbf{u})]1 \\
&+ [\mathscr{F}\{\mathbf{F}_1(\mathbf{x}) + \mathbf{F}_{23}(\mathbf{x})i_3\}(\mathbf{u})]\mathbf{e}_1 \\
&+ [\mathscr{F}\{\mathbf{F}_2(\mathbf{x}) + \mathbf{F}_{31}(\mathbf{x})i_3\}(\mathbf{u})]\mathbf{e}_2 \\
&+ [\mathscr{F}\{\mathbf{F}_3(\mathbf{x}) + \mathbf{F}_{12}(\mathbf{x})i_3\}(\mathbf{u})]\mathbf{e}_3.
\end{aligned}
\tag{37}
$$

The Fourier kernel consists of a scalar and a pseudoscalar or trivector. Considering the multiplication rules for a multiplication with them concludes this proof.

Note that dual pairs form Fourier pairs. The multivector space is divided into four orthogonal spaces which are then transformed separately. Because of Lemma (5.2), the 3D Clifford Fourier kernel commutes with every multivector (although Clifford multiplication is not generally commutative). All of the well-known theorems hold. Because of the non-commutativity of the Clifford multiplication, we present theorems for the application of a filter from the left and right.

Theorem 5.4 (Shift theorem) *Let $\boldsymbol{F} : \mathbb{R}^3 \to G_3$ be multivector valued and let $\mathscr{F}\{\boldsymbol{F}\}$ exist. Then*

$$\mathscr{F}\{\boldsymbol{F}(\boldsymbol{x}-\boldsymbol{x'})\}(\boldsymbol{u}) = \mathscr{F}\{\boldsymbol{F}\}(\boldsymbol{u})e^{(-2\pi\boldsymbol{i}_3\langle\boldsymbol{x'},\boldsymbol{u}\rangle)} . \tag{38}$$

Proof:

$$
\begin{aligned}
&\mathscr{F}\{\boldsymbol{F}(\boldsymbol{x}-\boldsymbol{x'})\}(\boldsymbol{u}) \\
=\ & \int_{\mathbb{R}^3} \boldsymbol{F}(\boldsymbol{x}-\boldsymbol{x'})e^{(-2\pi\boldsymbol{i}_3\langle\boldsymbol{x},\boldsymbol{u}\rangle)}|d\boldsymbol{x}| \\
=\ & \int_{\mathbb{R}^3} \boldsymbol{F}(\boldsymbol{k})e^{(-2\pi\boldsymbol{i}_3\langle\boldsymbol{k},\boldsymbol{u}\rangle)}e^{(-2\pi\boldsymbol{i}_3\langle\boldsymbol{x'},\boldsymbol{u}\rangle)}|d\boldsymbol{k}| \\
=\ & \int_{\mathbb{R}^3} \boldsymbol{F}(\boldsymbol{k})e^{(-2\pi\boldsymbol{i}_3\langle\boldsymbol{k},\boldsymbol{u}\rangle)}|d\boldsymbol{k}|e^{(-2\pi\boldsymbol{i}_3\langle\boldsymbol{x'},\boldsymbol{u}\rangle)} \\
=\ & \mathscr{F}\{\boldsymbol{F}\}(\boldsymbol{u})e^{(-2\pi\boldsymbol{i}_3\langle\boldsymbol{x'},\boldsymbol{u}\rangle)} .
\end{aligned}
\tag{39}
$$

Theorem 5.5 (Convolution theorem) *Let $\boldsymbol{F}, \boldsymbol{H} : \mathbb{R}^3 \to G_3$ be multivector valued and let $\mathscr{F}\{\boldsymbol{F}\}$ and $\mathscr{F}\{\boldsymbol{H}\}$ exist. Then*

$$
\begin{aligned}
\mathscr{F}\{\boldsymbol{H}*_l \boldsymbol{F}\}(\boldsymbol{u}) &= \mathscr{F}\{\boldsymbol{H}\}(\boldsymbol{u})\mathscr{F}\{\boldsymbol{F}\}(\boldsymbol{u}) \\
and \quad \mathscr{F}\{\boldsymbol{F}*_r \boldsymbol{H}\}(\boldsymbol{u}) &= \mathscr{F}\{\boldsymbol{F}\}(\boldsymbol{u})\mathscr{F}\{\boldsymbol{H}\}(\boldsymbol{u}).
\end{aligned}
\tag{40}
$$

Proof:

$$
\begin{aligned}
&\mathscr{F}\{\boldsymbol{H}*_l \boldsymbol{F}\}(\boldsymbol{u}) \\
=\ & \int_{\mathbb{R}^3} \left(\int_{\mathbb{R}^3} \boldsymbol{H}(\boldsymbol{x'})\boldsymbol{F}(\boldsymbol{x}-\boldsymbol{x'})|d\boldsymbol{x'}| \right) e^{(-2\pi\boldsymbol{i}_3\langle\boldsymbol{x},\boldsymbol{u}\rangle)}|d\boldsymbol{x}| \\
=\ & \int_{\mathbb{R}^3} \left(\int_{\mathbb{R}^3} \boldsymbol{H}(\boldsymbol{x'})\boldsymbol{F}(\boldsymbol{x}-\boldsymbol{x'})e^{(-2\pi\boldsymbol{i}_3\langle\boldsymbol{x},\boldsymbol{u}\rangle)}|d\boldsymbol{x'}| \right) |d\boldsymbol{x}| \\
=\ & \int_{\mathbb{R}^3} \left(\int_{\mathbb{R}^3} \boldsymbol{H}(\boldsymbol{x'})\boldsymbol{F}(\boldsymbol{x}-\boldsymbol{x'})e^{(-2\pi\boldsymbol{i}_3\langle\boldsymbol{x},\boldsymbol{u}\rangle)}|d\boldsymbol{x}| \right) |d\boldsymbol{x'}| \\
=\ & \int_{\mathbb{R}^3} \boldsymbol{H}(\boldsymbol{x'}) \left(\int_{\mathbb{R}^3} \boldsymbol{F}(\boldsymbol{x}-\boldsymbol{x'})e^{(-2\pi\boldsymbol{i}_3\langle\boldsymbol{x},\boldsymbol{u}\rangle)}|d\boldsymbol{x}| \right) |d\boldsymbol{x'}| \\
=\ & \int_{\mathbb{R}^3} \boldsymbol{H}(\boldsymbol{x'})e^{(-2\pi\boldsymbol{i}_3\langle\boldsymbol{x'},\boldsymbol{u}\rangle)}\mathscr{F}\{\boldsymbol{F}\}(\boldsymbol{u})|d\boldsymbol{x'}| \\
=\ & \int_{\mathbb{R}^3} \boldsymbol{H}(\boldsymbol{x'})e^{(-2\pi\boldsymbol{i}_3\langle\boldsymbol{x'},\boldsymbol{u}\rangle)}|d\boldsymbol{x'}|\mathscr{F}\{\boldsymbol{F}\}(\boldsymbol{u}) \\
=\ & \mathscr{F}\{\boldsymbol{H}\}(\boldsymbol{u})\mathscr{F}\{\boldsymbol{F}\}(\boldsymbol{u}) .
\end{aligned}
\tag{41}
$$

Because of the commutativity of the Clifford Fourier kernel, see Equation (5.2), the proof of the other cases is analog to the one above.

Theorem 5.6 (Derivative theorem) *Let the preconditions be the same as in 5.5. Then*

$$
\begin{aligned}
\mathscr{F}\{\nabla\boldsymbol{F}\}(\boldsymbol{u}) &= 2\pi\boldsymbol{i}_3\boldsymbol{u}\mathscr{F}\{\boldsymbol{F}\}(\boldsymbol{u}) , \\
\mathscr{F}\{\boldsymbol{F}\nabla\}(\boldsymbol{u}) &= \mathscr{F}\{\boldsymbol{F}\}(\boldsymbol{u})2\pi\boldsymbol{i}_3\boldsymbol{u} , \\
\mathscr{F}\{\Delta\boldsymbol{F}\}(\boldsymbol{u}) &= -4\pi^2\boldsymbol{u}^2\mathscr{F}\{\boldsymbol{F}\}(\boldsymbol{u}) , \\
and \quad \mathscr{F}\{\boldsymbol{F}\Delta\}(\boldsymbol{u}) &= -4\pi^2\boldsymbol{u}^2\mathscr{F}\{\boldsymbol{F}\}(\boldsymbol{u}) .
\end{aligned}
\tag{42}
$$

Proof: *Since*

$$
\begin{aligned}
(\nabla\boldsymbol{F})(\boldsymbol{x}) &= \nabla\mathscr{F}^{-1}\{\mathscr{F}\{\boldsymbol{F}\}\}(\boldsymbol{x}) \\
&= \nabla\int_{\mathbb{R}^3} \mathscr{F}\{\boldsymbol{F}\}(\boldsymbol{u})e^{(2\pi\boldsymbol{i}_3\langle\boldsymbol{x},\boldsymbol{u}\rangle)}|d\boldsymbol{x}| \\
&= \int_{\mathbb{R}^3} \nabla\left(\mathscr{F}\{\boldsymbol{F}\}(\boldsymbol{u})e^{(2\pi\boldsymbol{i}_3\langle\boldsymbol{x},\boldsymbol{u}\rangle)} \right) |d\boldsymbol{x}| \\
&= \int_{\mathbb{R}^3} \nabla\left(e^{(2\pi\boldsymbol{i}_3\langle\boldsymbol{x},\boldsymbol{u}\rangle)} \right) \mathscr{F}\{\boldsymbol{F}\}(\boldsymbol{u})|d\boldsymbol{x}| \\
&= \int_{\mathbb{R}^3} 2\pi\boldsymbol{i}_3\boldsymbol{u}e^{(2\pi\boldsymbol{i}_3\langle\boldsymbol{x},\boldsymbol{u}\rangle)}\mathscr{F}\{\boldsymbol{F}\}(\boldsymbol{u})|d\boldsymbol{x}| \\
&= \mathscr{F}^{-1}(2\pi\boldsymbol{i}_3\boldsymbol{u}\mathscr{F}\{\boldsymbol{F}\}(\boldsymbol{u}))
\end{aligned}
\tag{43}
$$

we get

$$\mathscr{F}\{\nabla\boldsymbol{F}\}(\boldsymbol{u}) = 2\pi\boldsymbol{i}_3\boldsymbol{u}\mathscr{F}\{\boldsymbol{F}\}(\boldsymbol{u}) \tag{44}$$

and

$$\mathscr{F}\{\Delta \boldsymbol{F}\}(\boldsymbol{u}) = 2\pi \boldsymbol{i}_3 \boldsymbol{u} \mathscr{F}\{\nabla \boldsymbol{F}\}(\boldsymbol{u}) = -4\pi^2 \boldsymbol{u}^2 \mathscr{F}\{\boldsymbol{F}\}(\boldsymbol{u}) . \tag{45}$$

The application of the derivative from the right can be proved analogously.

Theorem 5.7 (Parseval's theorem) *Let the preconditions be the same as in 5.4. Then*

$$\|\boldsymbol{F}\|_2 = \|\mathscr{F}\{\boldsymbol{F}\}\|_2 . \tag{46}$$

This is also true for the different grades of the multivector-valued signal $\boldsymbol{F}$ such that

$$\|\langle \boldsymbol{F}\rangle_j\|_2 = \|\mathscr{F}\{\langle \boldsymbol{F}\rangle_j\}\|_2, \; j = 0, .., 3 . \tag{47}$$

Proof: *The theorem for the classical Fourier transform is $\|f\|_2 = \|\mathscr{F}\{f\}\|_2$. The proof for the Clifford Fourier transform follows directly since the CFT is a linear combination of several classical Fourier transforms.*

5.3 Clifford Fourier transform in 2D

Definition 5.8 *Let $\boldsymbol{F} : \mathbb{R}^2 \to G_2$ be a multivector-valued signal. Let $x, u \in \mathbb{R}^2$. The* **Clifford Fourier transform** *(CFT) of $\boldsymbol{F}$ is defined as*

$$\mathscr{F}\{\boldsymbol{F}\}(\boldsymbol{u}) := \int_{\mathbb{R}^2} \boldsymbol{F}(\boldsymbol{x}) e^{(-2\pi \boldsymbol{i}_2 \langle \boldsymbol{x}, \boldsymbol{u}\rangle)} |d\boldsymbol{x}|. \tag{48}$$

The inverse transformation is then given by

$$\mathscr{F}^{-1}\{\boldsymbol{F}\}(\boldsymbol{x}) := \int_{\mathbb{R}^2} \boldsymbol{F}(\boldsymbol{u}) e^{(2\pi \boldsymbol{i}_2 \langle \boldsymbol{x}, \boldsymbol{u}\rangle)} |d\boldsymbol{u}|. \tag{49}$$

Note that this Clifford Fourier kernel $e^{(-2\pi \boldsymbol{i}_2 \langle \mathbf{x}, \mathbf{u}\rangle)}$ again consists of a scalar and a pseudoscalar. In G_2 this implies that the kernel is spinor-valued.

Theorem 5.9 *The Clifford Fourier transform is a linear combination of two classical Fourier transforms.*
Proof: *For a multivector field $\boldsymbol{F} : \mathbb{R}^2 \to G_2$, we have*

$$\boldsymbol{F} \;=\; \boldsymbol{F}_0 + \boldsymbol{F}_1 \boldsymbol{e}_1 + \boldsymbol{F}_2 \boldsymbol{e}_2 + \boldsymbol{F}_{12} \boldsymbol{e}_{12}, \tag{50}$$

which can be regarded as two complex signals

$$\begin{aligned}\boldsymbol{F}(\boldsymbol{x}) \;=\;& 1[\boldsymbol{F}_0(\boldsymbol{x}) + \boldsymbol{F}_{12}(\boldsymbol{x})\boldsymbol{i}_2] \\ +\;& \boldsymbol{e}_1[\boldsymbol{F}_1(\boldsymbol{x}) + \boldsymbol{F}_2(\boldsymbol{x})\boldsymbol{i}_2,]\end{aligned} \tag{51}$$

which can be interpreted as an element of $\mathbb{C}^2$. Considering the linearity of the Clifford Fourier transform, we get

$$\begin{aligned}\mathscr{F}\{\boldsymbol{F}\}(\boldsymbol{u}) \;=\;& 1[\mathscr{F}\{\boldsymbol{F}_0(\boldsymbol{x}) + \boldsymbol{F}_{12}(\boldsymbol{x})\boldsymbol{i}_2\}(\boldsymbol{u})] \\ +\;& \boldsymbol{e}_1[\mathscr{F}\{\boldsymbol{F}_1(\boldsymbol{x}) + \boldsymbol{F}_2(\boldsymbol{x})\boldsymbol{i}_2\}(\boldsymbol{u})]\end{aligned} \tag{52}$$

which means that the 2D Clifford Fourier transform is the linear combination of two classical Fourier transforms.

10

Again, dual pairs form Fourier pairs. This time, the Fourier kernel does not commute with every multivector, rather it commutes with the spinor part and anti-commutes with the vector part. Therefore, we present convolution theorems for vector and spinor-valued fields separately. Note also that the multiplication of the Fourier kernel from the right is not quite the same as that from the left as in 3D.

Theorem 5.10 (Shift theorem) *Let F be multivector valued and let $\mathscr{F}\{F\}$ exist. Then, we have*

$$\mathscr{F}\{F(x-x')\}(u) = \mathscr{F}\{F\}(u)e^{(-2\pi i_2\langle x',u\rangle)} . \tag{53}$$

Proof: *Analogous to the 3D equivalent (Theorem 5.4).*

Theorem 5.11 (Convolution theorem) *Let F,H be multivector valued, f,h be vector valued and $\mathfrak{f},\mathfrak{h}$ be spinor valued. Note that F,f and $\mathfrak{f}$ are fields and H,h and $\mathfrak{h}$ are filters. Let $\mathscr{F}\{F\}$, $\mathscr{F}\{H\}$, $\mathscr{F}\{f\}$, $\mathscr{F}\{h\}$, $\mathscr{F}\{\mathfrak{f}\}$ and $\mathscr{F}\{\mathfrak{h}\}$ exist. Then, we have*

$$
\begin{aligned}
\mathscr{F}\{H *_l \mathfrak{f}\}(u) &= \mathscr{F}\{H\}(u)\mathscr{F}\{\mathfrak{f}\}(u) , \\
\mathscr{F}\{H *_l f\}(u) &= \mathscr{F}\{\dot{H}\}(u)\mathscr{F}\{\dot{f}\}(u) , \\
\mathscr{F}\{F *_r \mathfrak{h}\}(u) &= \mathscr{F}\{F\}(u)\mathscr{F}\{\mathfrak{h}\}(u) , \\
and \quad \mathscr{F}\{F *_r h\}(u) &= \mathscr{F}\{\dot{F}\}(u)\mathscr{F}\{\dot{h}\}(u) .
\end{aligned}
\tag{54}
$$

Proof: *Let $\mathfrak{f}$ be spinor valued. Then we have*

$$
\begin{aligned}
&\mathscr{F}\{H *_l \mathfrak{f}\}(u) \\
&= \int_{\mathbb{R}^2} \left(\int_{\mathbb{R}^2} H(x')\mathfrak{f}(x-x')|dx'|\right) e^{(-2\pi i_2\langle x,u\rangle)}|dx| \\
&= \int_{\mathbb{R}^2} \left(\int_{\mathbb{R}^2} H(x')\mathfrak{f}(x-x')e^{(-2\pi i_2\langle x,u\rangle)}|dx'|\right) |dx| \\
&= \int_{\mathbb{R}^2} H(x') \left(\int_{\mathbb{R}^2} \mathfrak{f}(x-x')e^{(-2\pi i_2\langle x,u\rangle)}|dx|\right) |dx'| \\
&= \int_{\mathbb{R}^2} H(x')\mathscr{F}\{\mathfrak{f}\}(u)e^{(-2\pi i_2\langle x',u\rangle)}|dx'| \\
&= \int_{\mathbb{R}^2} H(x')e^{(-2\pi i_2\langle x',u\rangle)}|dx'|\mathscr{F}\{\mathfrak{f}\}(u) \\
&= \mathscr{F}\{H\}(u)\mathscr{F}\{\mathfrak{f}\}(u) .
\end{aligned}
\tag{55}
$$

Let f be vector valued, we have

$$
\begin{aligned}
&\mathscr{F}\{H \star_l f\}(u) \\
&= \int_{\mathbb{R}^2} \left(\int_{\mathbb{R}^2} H(x')f(x+x')|dx'|\right) e^{(-2\pi i_2\langle x,u\rangle)}|dx| \\
&= \int_{\mathbb{R}^2} \left(\int_{\mathbb{R}^2} H(x')f(x+x')e^{(-2\pi i_2\langle x,u\rangle)}|dx'|\right) |dx| \\
&= \int_{\mathbb{R}^2} H(x') \left(\int_{\mathbb{R}^2} f(x+x')e^{(-2\pi i_2\langle x,u\rangle)}|dx|\right) |dx'| \\
&= \int_{\mathbb{R}^2} H(x')\mathscr{F}\{f\}(u)e^{(2\pi i_2\langle x',u\rangle)}|dx'| \\
&= \int_{\mathbb{R}^2} H(x')e^{(-2\pi i_2\langle x',u\rangle)}\mathscr{F}\{f\}(u)|dx'| \\
&= \int_{\mathbb{R}^2} H(x')e^{(-2\pi i_2\langle x',u\rangle)}|dx'|\mathscr{F}\{f\}(u) \\
&= \mathscr{F}\{H\}(u)\mathscr{F}\{f\}(u) .
\end{aligned}
\tag{56}
$$

and therefore

$$\mathscr{F}\{H *_l f\}(u) = \mathscr{F}\{\dot{H}\}(u)\mathscr{F}\{\dot{f}\}(u) . \tag{57}$$

The other cases of the convolution theorem can be proved analogously.

Theorem 5.12 (Derivative theorem) *Let the preconditions be as in 5.11. Then, we have*

$$
\begin{aligned}
\mathscr{F}\{\nabla \boldsymbol{f}\}(\boldsymbol{u}) &= -2\pi \boldsymbol{i}_2 \boldsymbol{u} \mathscr{F}\{\boldsymbol{f}\}(\boldsymbol{u})\,, \\
\mathscr{F}\{\boldsymbol{f}\nabla\}(\boldsymbol{u}) &= 2\pi \boldsymbol{i}_2 \boldsymbol{u} \mathscr{F}\{\boldsymbol{f}\}(\boldsymbol{u})\,, \\
\mathscr{F}\{\nabla \boldsymbol{f}\}(\boldsymbol{u}) &= 2\pi \boldsymbol{i}_2 \boldsymbol{u} \mathscr{F}\{\boldsymbol{f}\}(\boldsymbol{u})\,, \\
\mathscr{F}\{\boldsymbol{f}\nabla\}(\boldsymbol{u}) &= 2\pi \boldsymbol{i}_2 \boldsymbol{u} \mathscr{F}\{\boldsymbol{f}\}(\boldsymbol{u})\,, \\
\mathscr{F}\{\boldsymbol{F}\nabla\}(\boldsymbol{u}) &= \mathscr{F}\{\boldsymbol{F}\}(\boldsymbol{u})(-2\pi \boldsymbol{i}_2 u)\,, \\
\mathscr{F}\{\Delta \boldsymbol{F}\}(\boldsymbol{u}) &= 4\pi^2 \boldsymbol{u}^2 \mathscr{F}\{\boldsymbol{F}\}(\boldsymbol{u})\,, \\
\text{and} \quad \mathscr{F}\{\boldsymbol{F}\Delta\}(\boldsymbol{u}) &= 4\pi^2 \boldsymbol{u}^2 \mathscr{F}\{\boldsymbol{F}\}(\boldsymbol{u})\,.
\end{aligned}
\tag{58}
$$

Proof: *For spinor **f**, the proof of the derivative theorem is analogous to that of (5.6). For vector valued **f**, we have*

$$
\begin{aligned}
(\nabla \boldsymbol{f})(\boldsymbol{x}) &= \nabla \mathscr{F}^{-1}\{\mathscr{F}\{\boldsymbol{f}\}\}(\boldsymbol{x}) \\
&= \nabla \int_{\mathbb{R}^2} \mathscr{F}\{\boldsymbol{f}\}(\boldsymbol{u}) e^{(2\pi \boldsymbol{i}_2 \langle \boldsymbol{x}, \boldsymbol{u}\rangle)} |d\boldsymbol{x}| \\
&= \int_{\mathbb{R}^2} \nabla \left(e^{(-2\pi \boldsymbol{i}_2 \langle \boldsymbol{x}, \boldsymbol{u}\rangle)} \mathscr{F}\{\boldsymbol{f}\}(\boldsymbol{u}) \right) |d\boldsymbol{x}| \\
&= \int_{\mathbb{R}^2} \nabla \left(e^{(-2\pi \boldsymbol{i}_2 \langle \boldsymbol{x}, \boldsymbol{u}\rangle)} \right) \mathscr{F}\{\boldsymbol{f}\}(\boldsymbol{u}) |d\boldsymbol{x}| \\
&= \int_{\mathbb{R}^2} -2\pi \boldsymbol{i}_2 \boldsymbol{u} e^{(-2\pi \boldsymbol{i}_2 \langle \boldsymbol{x}, \boldsymbol{u}\rangle)} \mathscr{F}\{\boldsymbol{f}\}(\boldsymbol{u}) |d\boldsymbol{x}| \\
&= \int_{\mathbb{R}^2} -2\pi \boldsymbol{i}_2 \boldsymbol{u} \mathscr{F}\{\boldsymbol{f}\}(\boldsymbol{u}) e^{(2\pi \boldsymbol{i}_2 \langle \boldsymbol{x}, \boldsymbol{u}\rangle)} |d\boldsymbol{x}| \\
&= \mathscr{F}^{-1}(-2\pi \boldsymbol{i}_2 \boldsymbol{u} \mathscr{F}\{\boldsymbol{f}\}(\boldsymbol{u}))
\end{aligned}
\tag{59}
$$

and

$$
\mathscr{F}\{\nabla \boldsymbol{f}\}(\boldsymbol{u}) = -2\pi \boldsymbol{i}_2 \boldsymbol{u} \mathscr{F}\{\boldsymbol{f}\}(\boldsymbol{u}).
\tag{60}
$$

Since ∇ is a vector and anti-commutes with the 2D Clifford Fourier kernel, the derivative theorem for the application of the derivative from the right can be proved analogously. Thus, we have

$$
\mathscr{F}\{\Delta \boldsymbol{F}\}(\boldsymbol{u}) = \mathscr{F}\{\boldsymbol{F}\nabla\}(\boldsymbol{u}) = 4\pi^2 \boldsymbol{u}^2 \mathscr{F}\{\boldsymbol{F}\}(\boldsymbol{u}).
\tag{61}
$$

Note that the frequency u is vector valued and anti-commutes with $\boldsymbol{i}_2$.

Theorem 5.13 (Parseval's theorem) *Let the preconditions be as in 5.10. Then, we have*

$$
\|\boldsymbol{F}\|_2 = \|\mathscr{F}\{\boldsymbol{F}\}\|_2.
\tag{62}
$$

Proof: *Analogous to the 3D equivalent (Theorem 5.7).*

6 EXAMPLES

6.1 Clifford Correlation

To demonstrate Clifford correlation, an ICE train travelling with a velocity of 250 km/h was chosen. The wind comes directly from the left. Due to the movement of the train, the angle of attack is 15 degree. The wind hits the ICE train front and left, and then rolls up on the right side of the train forming several vortices. A section plane with dimensions 51×51 through three of these vortices was computed (Figure 1), and used as an example of a simple flow with only a few features. Both flow topology and Clifford correlation with a rotational mask clearly depict the three vortices present in this section plane.
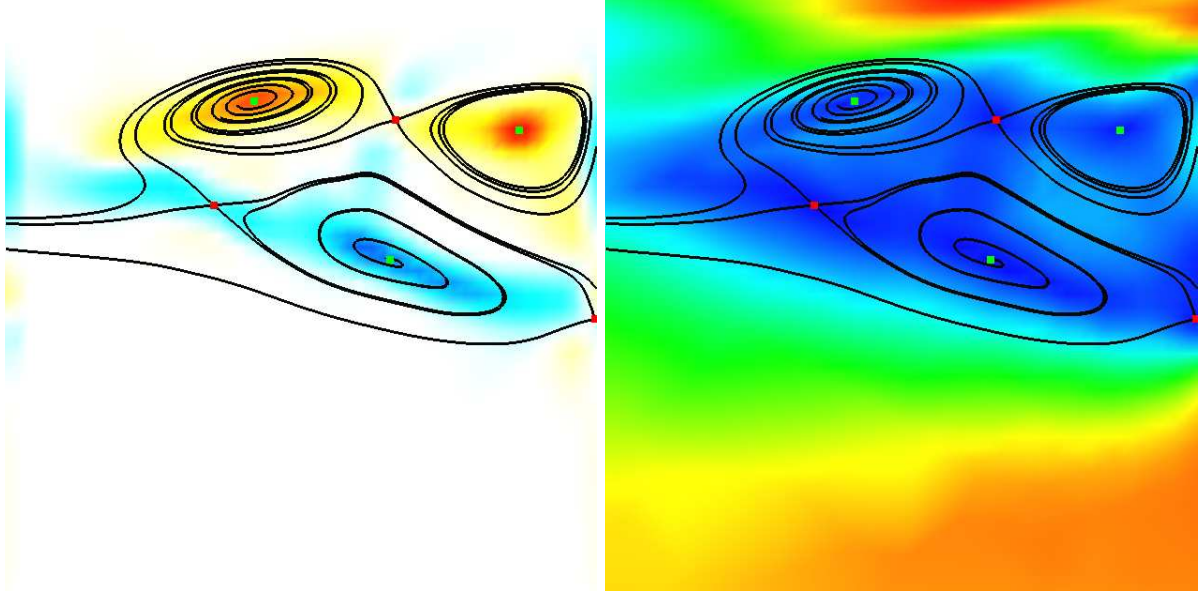
Figure 1: A section plane through vortices alongside an ICE train. **Left**: Topology, and results of Clifford correlation of the normalized data set, e.g. all vectors have same length, and a 5×5 rotational template. Color coding from dark blue (high negative similarity, clockwise rotation) to red (high positive similarity, counter-clockwise rotation). **Right**: Color-coding of the magnitude of the velocity from zero (blue) to high values (red), and topology. Note that the vortices are within an area of low velocity magnitudes.

6.2   Clifford Fourier Transform

The Clifford Fourier transform leads to the analysis of vector valued flow patterns in frequency domain. Therefore, the Clifford Fourier transforms of some 3D patterns (Figure 2) were studied. 3D patterns are easier to understand due to the interpretation of the 3D vector as three complex numbers in contrast to the 2D vector which is interpreted as only one complex number.

This split of the components of a 3D vector can be found in the DCFTs of the three patterns showing rotation and a saddle along one axis, and a convergence to a point (Figure 2). Rotation and saddle line, which are a repetition of the corresponding 2D pattern along the third axis, have no non-zero Clifford Fourier coefficients corresponding to this third direction as the values do not change in this direction. The DCFT of the convergence, on the other hand, has non-zero coefficients for the third direction as convergence takes also place in this direction.

Note that all patterns are real valued. Thus, the real or vector valued parts of DCFTs are symmetric, that is $\langle \mathscr{F}\{f\}(u)\rangle_1 = \langle \mathscr{F}_r\{f\}(-u)\rangle_1$. The imaginary or bivector parts are antisymmetric, $\langle \mathscr{F}_i\{f\}(u)\rangle_2 = -\langle \mathscr{F}_i\{f\}(-u)\rangle_2$. This is in contrast to the visual perception of these patterns, which would rate the vector part as antisymmetric and the bivector part as symmetric due to the orientation of the vectors. However, this visual perception of the symmetry of vector fields is in contrast to the mathematical definition of symmetry and antisymmetry.

The interpretation of the DCFTs of these patterns is odd at first. A careful distinction between the direction of the waveforms, and the direction of the resulting vectors given by the component of the vector in which the waveform is present, has to be made. An example is the DCFT of the rotation. The rightmost vector and bivector correspond to the waveform with direction x. As the vector is $a\mathbf{e}_2 = ay$ and the bivector $-bi\mathbf{e}_2 = -biy$, the wave is in the second component of the vector. Out of the complex number $(a - ib)$ corresponding to the second component of the multivectors, the amplitude and phase of the signal in this component of the vector can be determined. Note that for the determination of the properties of this waveform, the leftmost
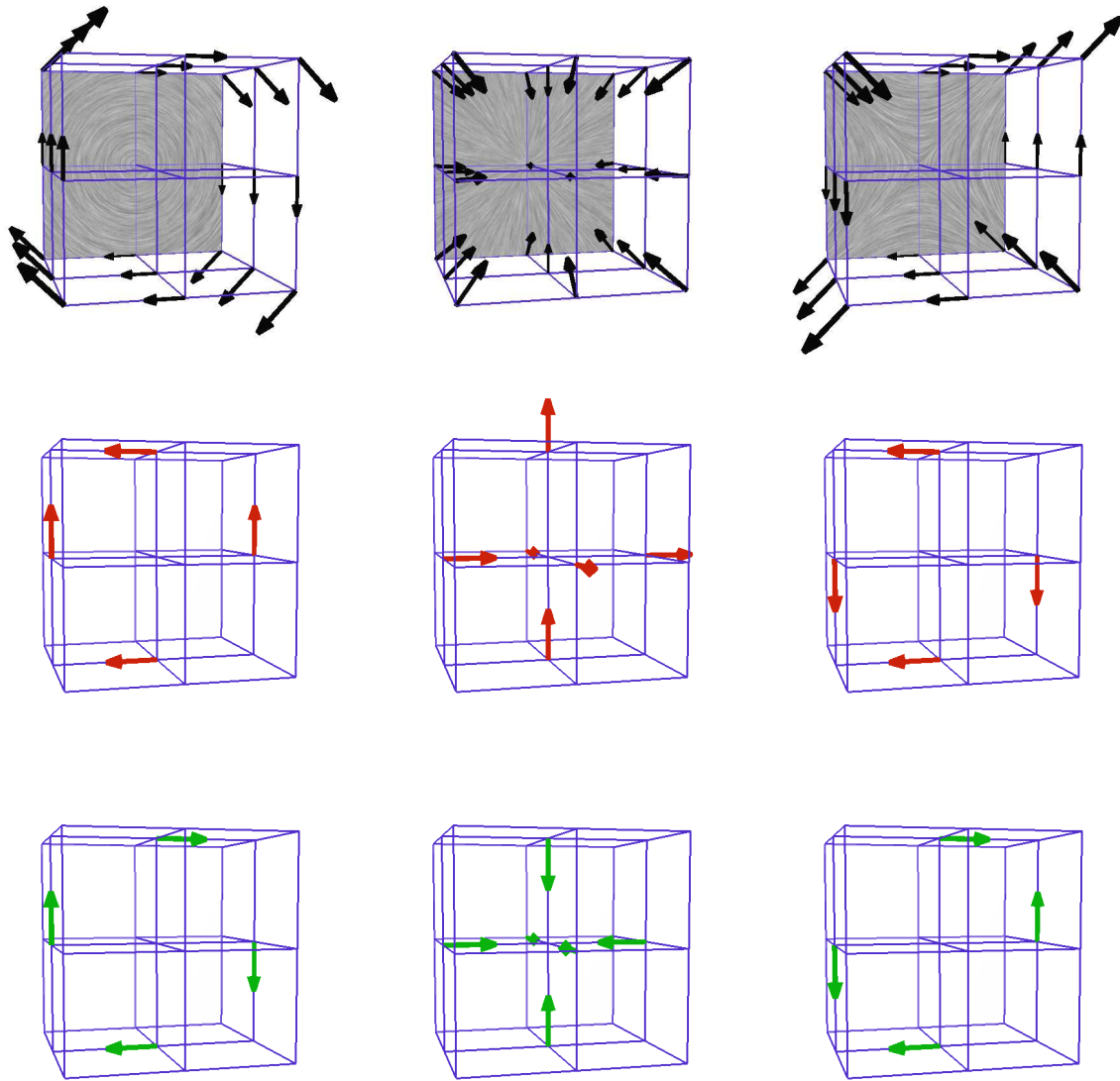
13

Figure 2: **Top**: Various 3D patterns. **Middle**: The vector part of their DCFT. **Bottom**: The bivector part of their DCFT, displayed as normal vector of the plane. **Left**: $3 \times 3 \times 3$ rotation in one coordinate plane. **Middle**: $3 \times 3 \times 3$ convergence. **Right**: $3 \times 3 \times 3$ saddle line. The mean value of the DCFT is situated in the center of the field. In 3D, the waves forming the patterns can be easily seen in the frequency domain. The magnitude of the bivectors of the DCFT is only half the magnitude of the corresponding vectors, though both are displayed with same length.

vector and bivector can be ignored due to symmetry properties.

6.3 Fast Clifford Fourier Transform

One of the reasons the Fourier transform is so successful in image processing is the existence of fast Fourier transforms (FFT). Algorithms for the fast computation of the Fourier transform take a divide and conquer approach based on recursively dividing even and odd elements. The basic approach assumes that the dimensions of the images are of the form 2^k. Since the Clifford Fourier Transform can be computed as a linear combination of several regular Fourier transforms, FFT-like algorithms can be applied directly for acceleration of the CFT. The Clifford Fourier transforms for Figure 3 have been computed using a fast Clifford Fourier transform.

Thus, the computational time of the CFT for this data set was reduced from hours to mere seconds.

For vector-valued data we chose a turbulent swirling jet entering a fluid at rest. The simulation consists of a cylinder and a planar cut along the axis of the cylinder defines the domain. The domain has been discretized by a 124×101 rectilinear grid with smaller rectangles near the cylinder axis. Since several small and large vortices are present in the flow, a discrete numerical simulation (DNS), using a higher order finite difference scheme, was used to solve the incompressible Navier-Stokes equations. For demonstration of the fast Clifford Fourier transform, we performed a uniform resampling of the grid having dimensions of $256 \times 128 = 2^8 \times 2^7$. Note that the resampled data set is smaller in height than the original one. Figure 3 shows the application of a fast discrete Clifford Fourier transform to the resampled field. A 2D vector field transforms into a 2D vector field since it forms one complex signal. A 3D vector field
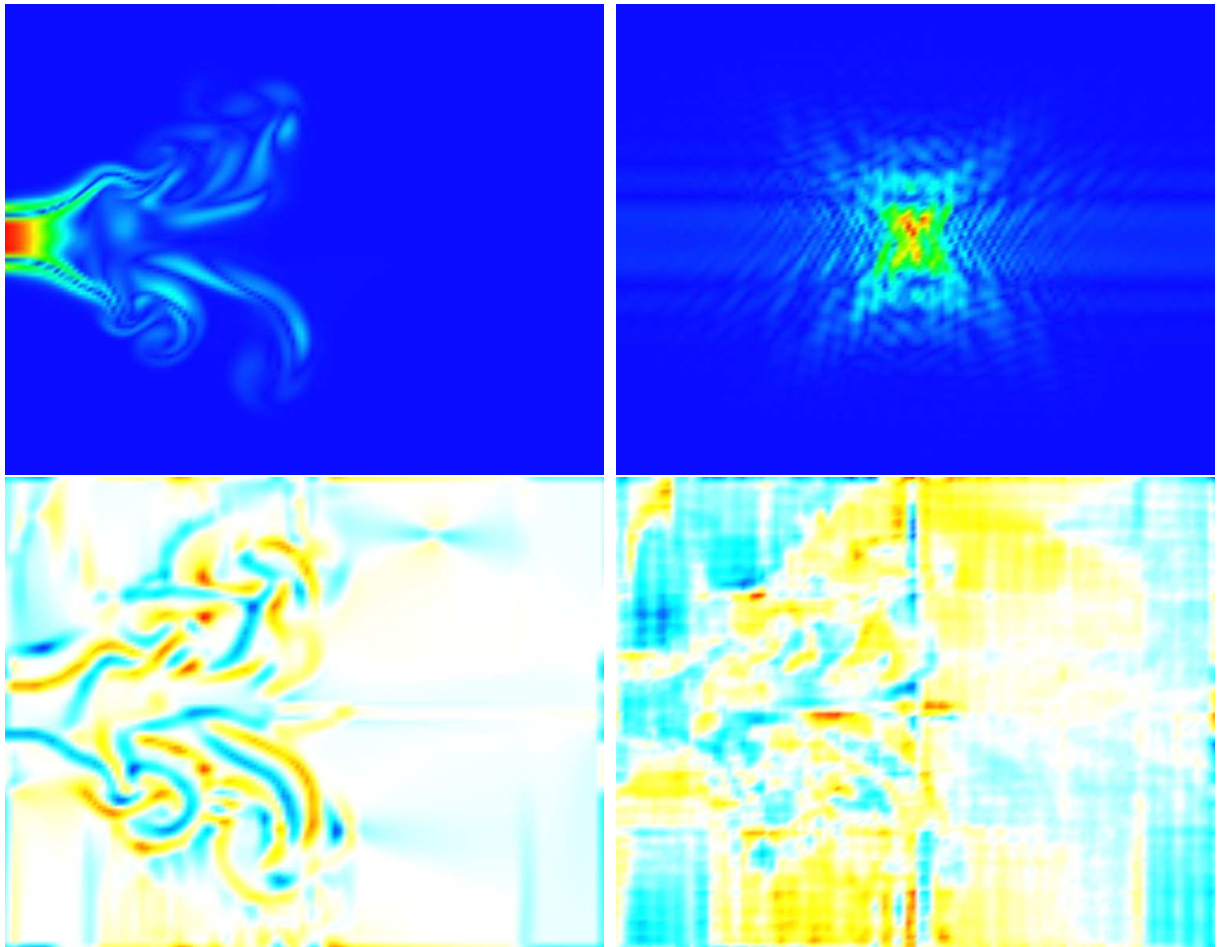
Figure 3: Swirling jet entering fluid at rest. **Top left**: Color coding of the absolute magnitude of the vectors. The colors are scaled from zero (blue) to the maximal magnitude (red). **Top right**: (Fast) Discrete Clifford Fourier transform of the dataset. Zero frequency is located in the middle of the image. Vectors transform to multivectors when using Clifford algebra in frequency domain, thus, color coding is based on the magnitude of the multivectors. Scaling of the colors is the same as the left image. **Bottom left**: Correlation with a counter-clockwise 5×5 rotational pattern. The data set has been normalized to emphasize small structures. The image shows correlation computed in frequency domain with the result transformed back to spatial domain. Color coding of the scalar part is blue for high negative similarities (-0.94) and a left-handed rotation and red for high positive similarities (0.94) and a right-handed rotation. **Bottom right**: Difference in the computation of the correlation operation in spatial domain using a periodic boundary condition. The colors are scaled from -1×10^{-13} (blue) to 1×10^{-13} (red).

transforms into a multivector field with vector and bivector parts nonzero.

7 APPLICATION

7.1 Similarity Value

As used by Heiberg et al. [14], the similarity of two vector-valued patterns is defined by the sum of the scalar products of their vectors:

$$s(\mathbf{x}) = \langle (\mathbf{h} * \mathbf{f})(\mathbf{x}) \rangle_0 \qquad (63)$$

The similarity value itself depends on the magnitude of both the patterns in the field and the template itself. Therefore, the obtained similarity values are usually scaled by the magnitude of the template pattern:

$$s(\mathbf{x}) = \frac{(\mathbf{h} * \mathbf{f})(\mathbf{x})}{\sum_{\mathbf{x'} \in \mathbf{h}} |\mathbf{h}(\mathbf{x'})|} \qquad (64)$$

Often, this similarity is influenced more by the velocity of the vectors than their orientations. Then, it can be sensible to normalize the similarity by the velocities of the pattern in the data set as well. It can be achieved quite easily by unifying the vector magnitudes of the field beforehand. Matching on a data set thus normalized corresponds to a matching of the streamlines rather than the vectors themselves (Figure 4).
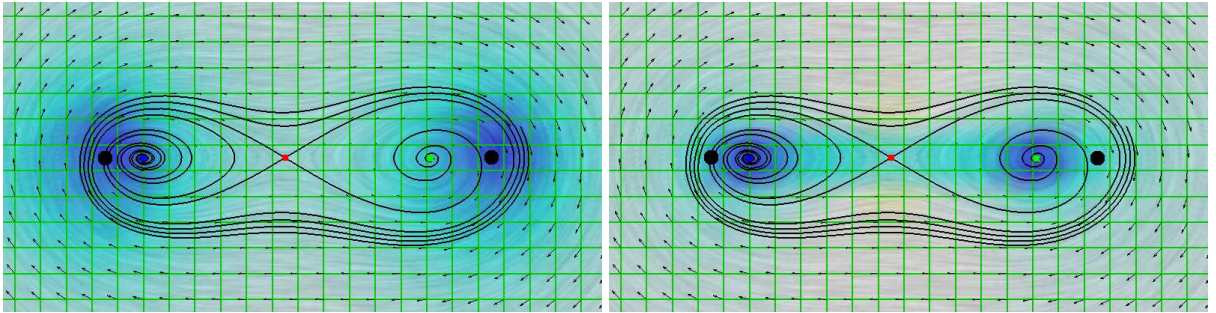
Figure 4: Superposition of two Vatistas vortices [30] with both radius 5, radial velocity 1 and N=1. The original vortex centers are displayed (black dots) as well as the grid (green) and hedgehogs (black arrows). Color coding of similarity values from high negative values (blue) to high positive values (red). **Left**: Template matching with a 3×3 rotational mask detects the true vortex centers. **Right**: Normalizing the field and matching afterwards yields results more similar to streamline behavior.

7.2 Rotation Invariant Matching

The angle between the directions of the template and the structure in the field can be computed by a Clifford correlation. A basic idea for a rotation invariant matching algorithm would thus be to rotate the template into this direction, and compute one Clifford correlation for the similarity.

As annihilation effects the approximation of the direction, it is not enough to compute only one Clifford correlation for stable results. Thus, additional templates with different directions have to be used [8]. A possible template distribution, which results in a stable, rotation invariant matching algorithm, is:

1. 2D: $a = 0.5$ and $b = \frac{\sqrt{3}}{2}$

16

$$\mathbf{n}_1 = (1,0)^T$$

$\mathbf{n}_2 = (-a, b)^T$, that is $\mathbf{n}_1$ rotated 120° counterclockwise.

$\mathbf{n}_2 = (-a, -b)^T$, that is $\mathbf{n}_1$ rotated 240° counterclockwise.

2. 3D: The directions of the principal axes of the coordinate system are used:

$$\mathbf{n}_1 = (1,0,0)^T, \mathbf{n}_2 = (-1,0,0)^T,$$
$$\mathbf{n}_3 = (0,1,0)^T, \mathbf{n}_4 = (0,-1,0)^T,$$
$$\mathbf{n}_5 = (0,0,1)^T, \mathbf{n}_6 = (0,0,-1)^T,$$

The algorithm also works with other directions and other numbers of directions. As usual, one can trade precision for computational speed. The templates are rotated in the desired direction using Clifford algebra and linear interpolation.

For an easier computation of the angles unhindered by the magnitudes of the vectors, both vector fields are normalized. Then, correlation with each rotated template is computed. Now, the approximations $\mathbf{n'}_k(\mathbf{x})$ of the direction of the structure in the field at $\mathbf{x}$ given by the correlations with the different templates are computed. Out of these directions, a single direction $\mathbf{n'}(\mathbf{x})$ has to be determined. In 2D, the template response with the smallest angle to the structure can be used directly. In 3D, the direction is computed analog to the computation of a center of gravity. Only the directions $\mathbf{n'}_k$ calculated out of the template responses $(\mathbf{h} \star \mathbf{f})(\mathbf{x})$ with scalar part $\langle (\mathbf{h} \star \mathbf{f})(\mathbf{x}) \rangle_0 \geq 0$ are used, as they point into the right hemisphere. These directions are weighted with the scalar part of their filter response. The resulting vector is normalized and gives the direction $\mathbf{n'}$ of the structure. For patterns which are rotational symmetric for all rotation directions, this approach can fail as all filter responses will result in the same similarity value. This has to be considered in the implementation, simple queries concerning the similarity values can detect this case. For these structures, any direction is correct, so the original direction of the template can be chosen.

In a last step, the template is rotated into the computed direction, and another vector correlation is computed as the final similarity value. Note that for this last vector correlation, field and template need not be normalized.

7.3 Determination of Parameters

This far, the similarity values are only given at the nodes of the grid, and local maxima of the similarity determine existence and position of the features. To get subpixel accuracy, two different methods are proposed here. First of all, the center of similarity can be computed:

Definition 7.1 *Let $\mathbf{p}(i)$ denote the positions in Ω, and let $s(i)$ be the similarity value at $\mathbf{p}_i$. Then the center of similarity (CoS) of Ω is defined as*

$$CoS = \frac{\sum_i \mathbf{p}(i) * s(i)}{\sum_i \mathbf{p}(i)}.$$

CoS result in exactly the same positions. To determine the neighborhood before the CoS computation automatically, the size of the feature (without subpixel accuracy) should be approximated first. The region thus defined, or a multiple thereof, can be used before the computation of CoS.

Another approach is to use a kind of bisection method. Note that linear interpolation, which is most often used in grids, can be computed via a convolution with a triangle filters and that
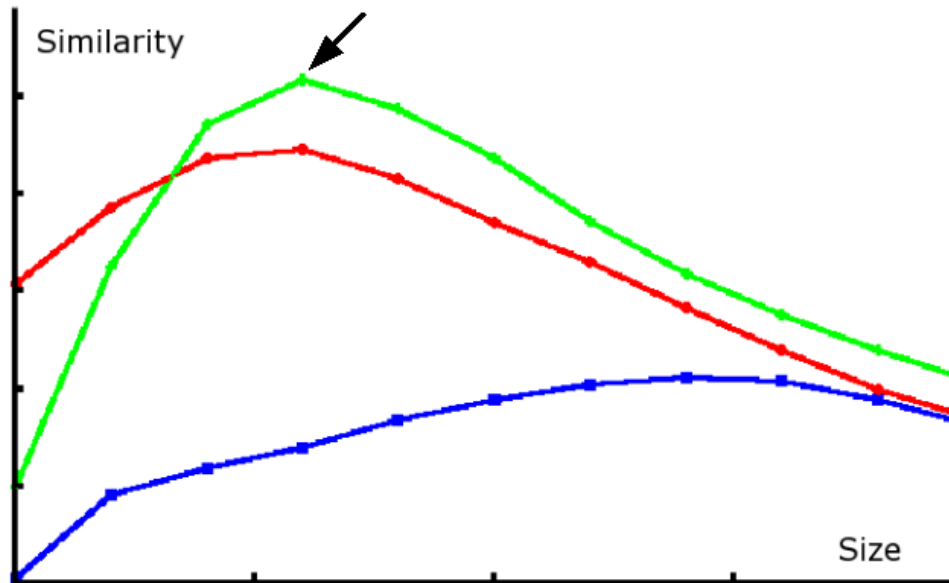
Figure 5: Similarity with a pure rotational template (y-axis) vs. template size (x-axis) for three positions. Shown are the position with maximal similarity to the 5^2 rotational template (red), the template with maximal similarity within the size computation (green), and the position with maximal template size within the region defined by a percentage threshold (blue). The maximal similarity of the green line (black arrow) determines position and size of the vortex.

(scalar) convolutions are commutative. That means that computing the similarity at an arbitrary point in a cell of the grid results in the same value as computing the similarity at the nodes and then interpolating the results. Thus, the maximal similarity can only be at a grid node. However, templates can be generated with the rotation center at every arbitrary point in space. So, the template is not moved for subpixel accuracy, but the center of the features within the template. It has the disadvantage that the template has to be computed for every new position, but the similarity values of different subpixel positions are nearly equal within a few iterations. This bisection method needs less data than CoS. For simple test cases, if the neighborhood for the CoS computation is large enough and well behaved, the bisection method is less precise. As soon as the data becomes complex, the bisection method produces results which are more reasonable than the CoS approach.

Another issue which should not be neglected is the connection between scale and position, computing the position of a feature at different scales can yield quite different results. Thus, position and size can only be determined accurately when their detection is coupled. The computation of the size of the feature should be done within a small region of the assumed center of the feature. The region can be detected automatically by using all positions in the neighborhood which have similarity measures above a certain percentage of the maximal similarity value. There is a relationship between computational effort and a stable threshold, but the regions are not that large, and, for example, 33% gives stable results for all datasets tested. The position which gave the largest similarity in the computation of the size of the feature is the grid node next to the true center of the feature and thus both determine the position, though not with subpixel accuracy, and the size of the feature. It is not automatically the position where the maximal size was computed as can be seen in Figure 5. Note that it is not sensible to determine subpixel accuracy of position and size before the true center has thus been identified.

Again, the size is only determined with an accuracy of edge length so far. For subpixel accuracy, the trick from the last subsection has to be used again. Here, this means that the size

18

of the template stays the same but the assumed core radius is changed. This way, an accuracy of one tenth of the edge length can be achieved.

For the example of a vortex, the previous parameters can be determined using a pure rotational template. For subpixel accuracy of the size, this is no longer optimal. A Rankine [21] template, with linear behavior within the vortex core and exponential drop-off outside, behaves not bad. However, for subpixel accuracy, the velocity at the core radius should be enlarged to get a significant drop-off in the similarity values once the radius is bigger than the vortex core radius. Another possibility is to use only the vectors within half an edge or less of the core radius and zero the rest. With this template, the velocity at the core radius v_r can be read of directly from the similarity values. Because of the averaging, the result is a little bit smaller than the actual values, but not significantly.

7.4 Application I - HART II

In 2001, a major international cooperative research program was conducted to investigate the physics of blade pressure, noise radiation, and vibrations caused by the wake of helicopter rotors [3, 29]. Concurrently, a comprehensive experimental database for code development and validation has been generated. There are three major sources for blade pressure fluctuations, noise and vibrations – the superposition of flight speed and blade rotation, the aerodynamic interference between the rotor and the main body of the helicopter, and the wake vortices of the rotor hitting other blades. This research program concentrates on the latter phenomena. It is called HART II for Higher-harmonic-control (HHC) Aeroacoustics Rotor Test II and it is a follow up on the HART program of 1994. (HHC describes the process of influencing the blade pitch angle, 3,4 or 5 times per revolution, to reduce noise and vibration.) The German DLR, the French ONERA, the Netherlands DNW, the US Army Aeroflightdynamics (AFDD) and NASA Langley all take part in the cooperation.

Three-component Particle Image Velocimetry (3-C PIV) [20] were part of the measurements. These resulted in 3-component vector fields on a 2D uniform grid describing the flow in the wake of the rotor within one image plane (Figure 6). To understand the wake of the rotor blades, and to be able to create a model of it, all vortices and other features have to be detected and their parameters have to be determined as precisely as possible. For accurate determination of the parameters, superposition effects and their consequences for the accuracy of the analysis methods have to be taken into account.

Using Clifford correlation on this data is advantageous. First of all, the data is already aligned on a uniform grid. As these vector fields were gained by measurements, the amount of noise present in the data presents a problem for many analysis methods. Due to the averaging of the integral, Clifford correlation is robust in terms of noise. And last but not least, as correlation with a template is a linear, shift invariant system, the proposed approach is inherently suited to approximate the flow with simpler, abstract models of vortices and other features. Some results can be seen in Figure 7.

7.5 Application II - Gas Furnace Chamber

An interesting flow data set is a gas furnace chamber as it is used for heating a house. The simulation solves compressible Navier-Stokes equations using a turbulent model applied on an irregular grid consisting of 174341 tetrahedra with 32440 vertices. For template matching, the data was resampled onto a uniform grid with dimensions $126 \times 65 \times 57$. In Figure 8, top, the swirling gas enters the chamber in the center of the left face while the air enters from 9 openings
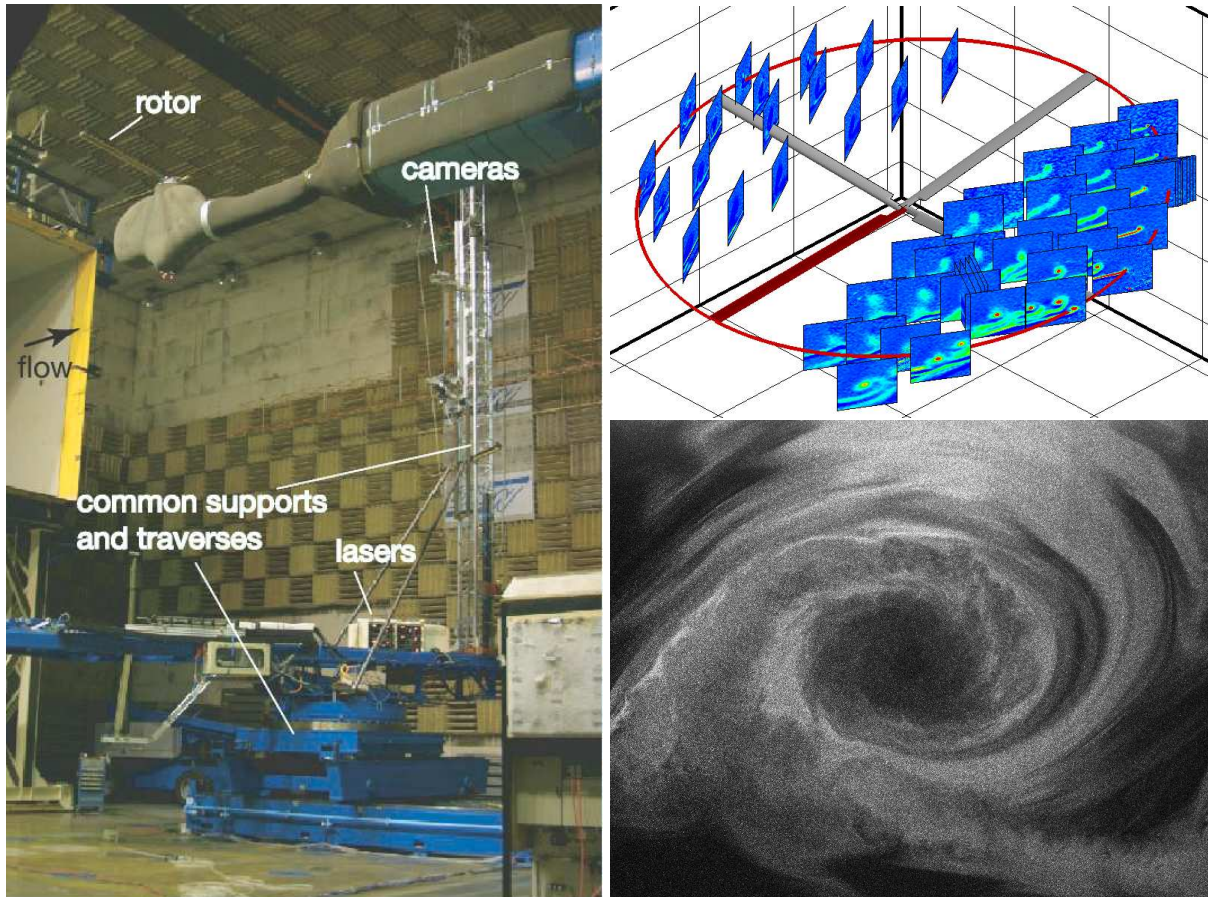
Figure 6: The HART II test. **Left**: Measurement configuration of the helicopter model in the wind channel. **Right top**: PIV measurement positions in the wake of the helicopter rotor blades. The red blade is at the rear position, and the wind comes from the right. **Right bottom**: A raw PIV image. Out of a stereo pair of these images, 3-C vector fields are computed. All figures courtesy of DLR Braunschweig.

on the top and 9 openings on the bottom, so that the combustion takes place in the center area of the chamber. The products of the combustion leave the chamber on the right. The flow is highly turbulent and exhibits a lot of different scale vortices. This is desirable, as the combustion will be more efficient the longer gas and air mix.

The structures in the flow can easily be identified by a segmentation of the flow based on Clifford correlation (Figure 8, bottom). Note that the shear flow at the front bottom (in yellow) is a misclassification, it is actually an elliptical vortex. This is one reason why the vortex core itself (in red) extends into this area. Note also the saddle line behind these vortices (in green), it is clearly visible in the bottom image.

Additional information of the gas furnace chamber can be gained by displaying an isosurface of the velocity of the original data set (Figure 8, blue isosurface). Using this isosurface, the gas and air inflow streams are clearly visible. Note the vortices besides them, and how they follow the shape of adjacent air streams.

8 CONCLUSION

Clifford convolution and correlation provide a technique for templates matching of vector fields as well as a unified notation for further processing including scalar-valued data. A Clif-
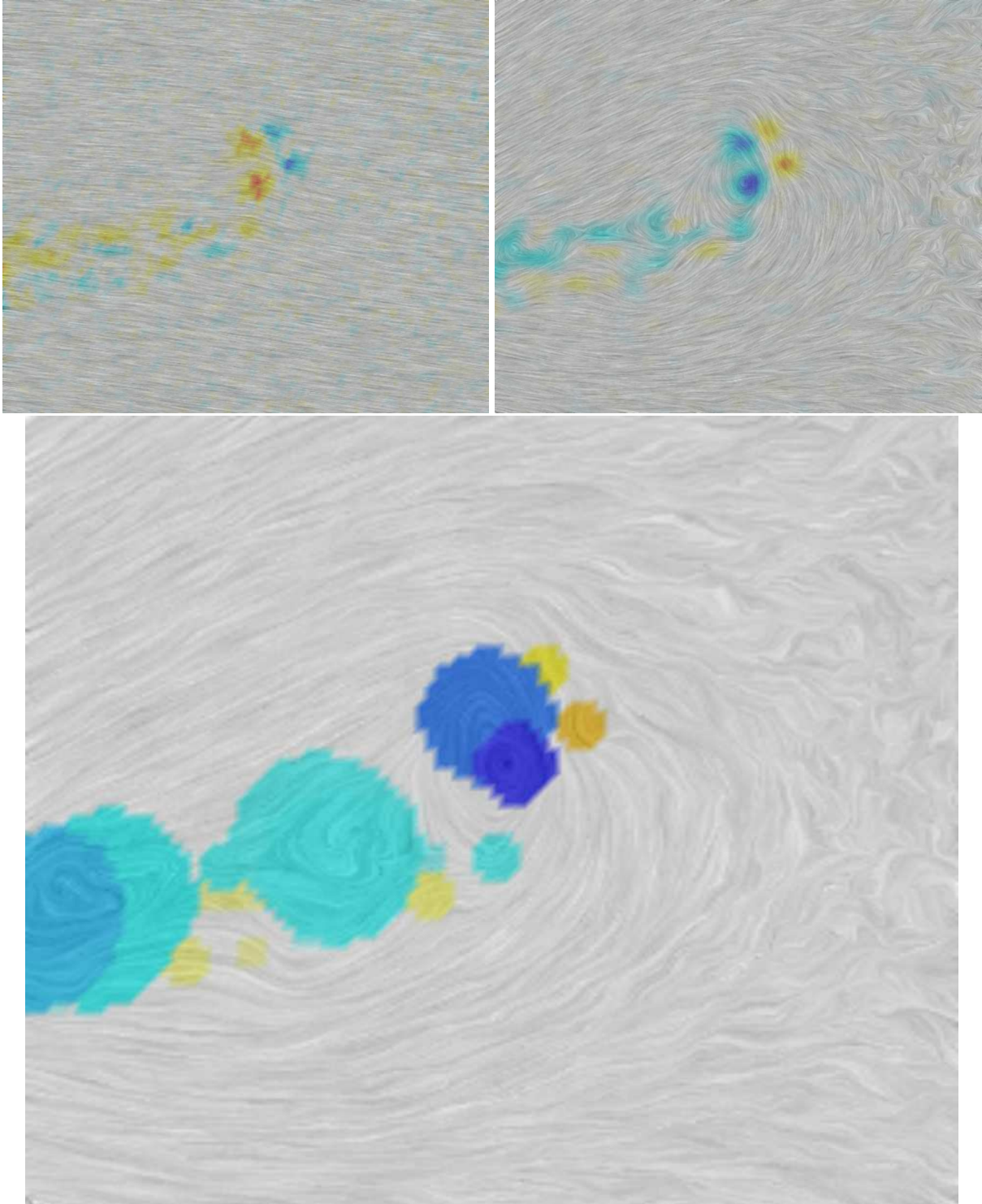
Figure 7: One vector field of the HART II test. **Top left**: LIC and Vorticity. The flow-through component hides all features. Vorticity is Galilean invariant and thus detects the vortices. **Top right**: LIC of the flow with average removed shows only one vortex. The similarity to a 5^2 rotational template, where blue denotes high similarity to a counter-clockwise rotation and red a high similarity to a clockwise rotation, is shown. The results are similar to a smoothed version of the vorticity. **Bottom**: Position and size of all detected vortices. Blue denotes high similarity to a counter-clockwise rotation and red a high similarity to a clockwise rotation. The recently produced tip vortex has the highest similarity and a small size, and the vortices in the wake area in the left of the image are weak.
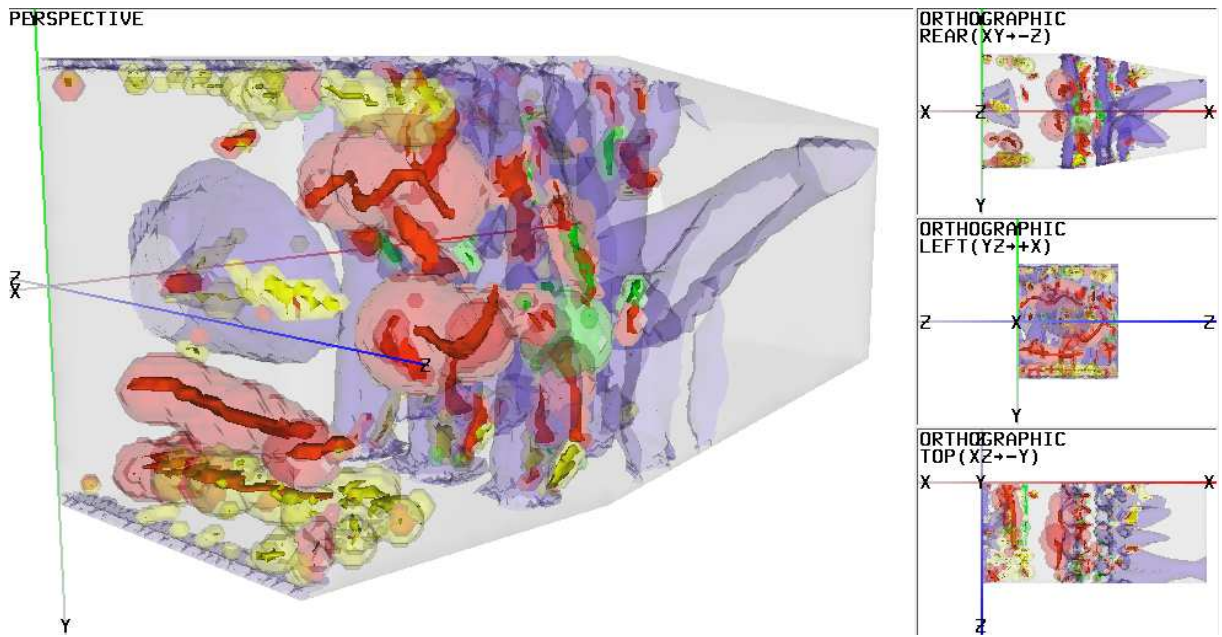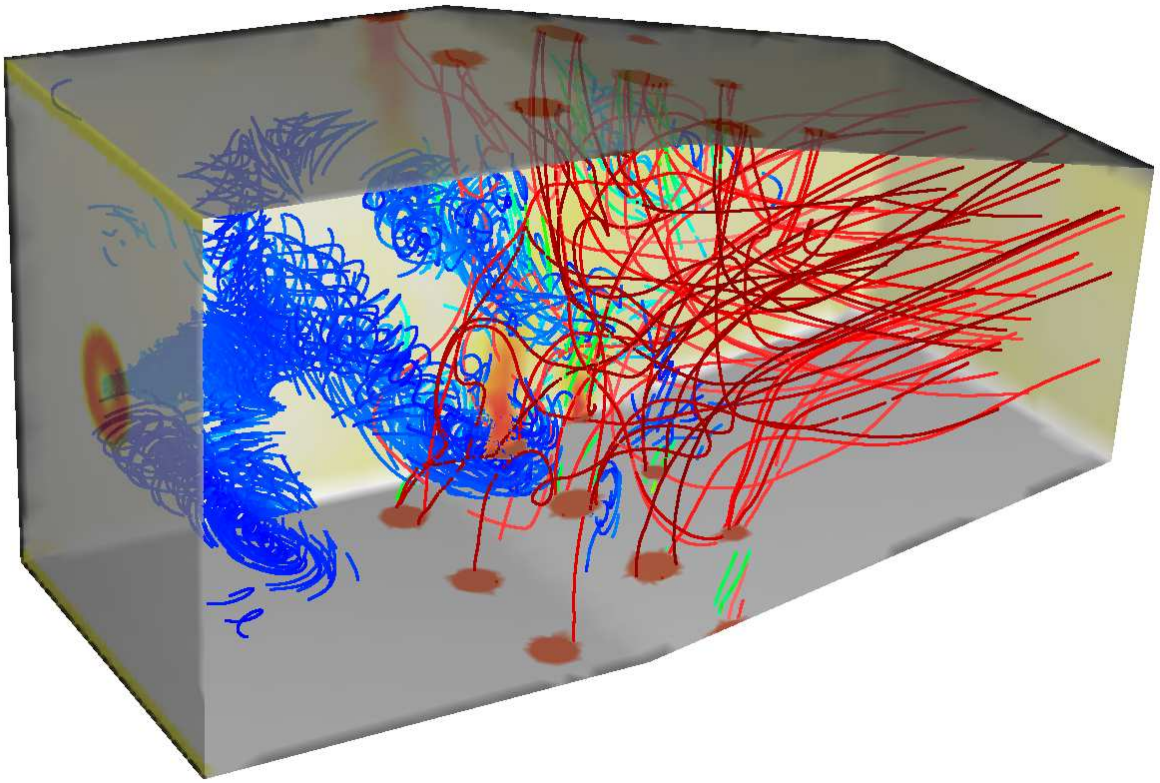
Figure 8: A gas furnace chamber. **Top**: Color coding of the velocity of the boundary to show the inflow areas. Streamlines (red) started at the top and bottom gas inflow. The gas leaves the chamber in the rear. Streamlines (blue) seeded by matching results of a 5x5x5 rotational template (threshold 0.5) display large vortices. **Bottom**: Segmentation of the normalized gas furnace chamber. Isosurfaces of the results (value 0.5): Red: rotations, yellow: shear flow, green: saddles. The cores of the regions are also displayed. The velocity of the original data set is displayed at an isovalue of 15 in blue.

ford Fourier transform has been defined for 2D and 3D, the common cases in flow fields. The corresponding theorems extend those applicable to the Fourier transform on scalar fields while still remaining reasonably simple. The existence of fast algorithms for the computation of the Clifford Fourier transform as well as a convolution theorem allow an acceleration of Clifford convolution and related template matching algorithms. Furthermore, analyzing flow pattern in frequency domain allows new insights into the flow. Template matching based on Clifford correlation has been successfully applied for the detection and analysis of flow features in several complex data sets. Thus, a major step towards robust and automatic detection, analysis and visualization of flow fields has been taken.

ACKNOWLEDGMENTS

REFERENCES

[1] F. Brackx, N. De Schepper, and F. Sommen. The Clifford-Fourier Transform. *The Journal of Fourier Analysis and Applications*, 11(6), 2005.

[2] T. Bülow. *Hypercomplex Spectral Signal Representations for the Processing and Analysis of Images*. PhD thesis, University of Kiel, Germany, 1999.

[3] C. L. Burley, T. F. Brooks, B. G. van der Wall, H. Richard, M. Raffel, P. Beaumier, Y. Delrieux, J. W. Lim, Y. H. Yu, C. Tung, K. Pengel, and E. Mercker. Rotor Wake Vortex Definition - Initial Evaluation of Results of the HART-II Study. In *28th EUROPEAN ROTORCRAFT FORUM*, Bristol, England, 2002.

[4] C. L. Burley, T. F. Brooks, B. G. van der Wall, H. Richard, M. Raffel, P. Beaumier, Y. Delrieux, J. W. Lim, Y. H. Yu, C. Tung, K. Pengel, and E. Mercker. Rotor Wake Vortex Definition Using PIV Measurements - Corrected for Orientation. In *9th AIAA/CEAS Aeroacoustics Conference*, 2003.

[5] B. Cabral and L. C. Leedom. Imaging Vector Fields Using Line Integral Convolution. In *Proceedings of SIGGRAPH '93*, pages 263–270, New York, 1993.

[6] W.C. de Leeuw and R. van Liere. Visualization of Global Flow Structures Using Multiple Levels of Topology. In E. Gröller, H. Löffelmann, and W. Ribarski, editors, *Data Visualization '99 (Proceedings VisSym '99)*, pages 45–52, 1999.

[7] H. Doleisch, M. Gasser, and H. Hauser. Interactive Feature Specification for Focus+Context Visualization of Complex Simulation Data. In *Proceedings of the 5th Joint IEEE TCVG - EUROGRAPHICS Symposium on Visualization (VisSym 2003)*, pages 239–248, Grenoble, France, 2003.

[8] J. Ebling and G. Scheuermann. Clifford Convolution and Pattern Matching on Vector Fields. In *Proceedings of IEEE Visualization 2003*, pages 193–200, Los Alamitos, CA, 2003. IEEE Computer Society.

[9] J. Ebling and G. Scheuermann. Fourier Transform on Multivector Fields. *IEEE Transactions on Visualization and Computer Graphics*, 11(4):469–479, 2005.

[10] J. Ebling and G. Scheuermann. Segmentation of Flow Field using Pattern Matching. In *Data Visualization 2006*, 2006.

[11] J. Ebling, G. Scheuermann, and B.G. van der Wall. Analysis and Visualization of 3-C PIV Images from HART II using Image Processing Methods. In *Data Visualization 2005*, pages 161–168, 2005.

[12] M. Felsberg. *Low-Level Image Processing with the Structure Multivector*. PhD thesis, University of Kiel, Germany, 2002.

[13] G. H. Granlund and H. Knutsson. *Signal Processing for Computer Vision*. Kluwer Academic Publishers, 1995.

[14] E. B. Heiberg, T. Ebbers, L. Wigström, and M. Karlsson. Three Dimensional Flow Characterization using Vector Pattern Matching. *IEEE Transactions on Visualization and Computer Graphics*, 9(3):313–319, 2003.

[15] J.L. Helman and L. Hesselink. Visualizing Vector Field Topology in Fluid Flows. *IEEE Computer Graphics and Applications*, pages 36–46, 1991.

[16] B. Jähne. *Digitale Bildverarbeitung*. Springer Verlag, Berlin, Germany, 2002.

[17] A. K. Jain. *Fundamentals of Digital Image Processing*. Prentice Hall, Englewoods Cliffs, NJ, USA, 1989.

[18] D. N. Kenwright, C. Henze, and C. Levit. Feature Extraction of Separation and Attatchment Lines. *IEEE Transactions on Visualization and Computer Graphics*, 5(2):151–158, 1999.

[19] F. H. Post, B. Vrolijk, H. Hauser, R. S. Laramee, and H. Doleitsch. The State of the Art in Flow Visualization: Feature Extraction and Tracking. *Computer Graphics Forum*, 22(4):775–792, 2003.

[20] M. Raffel, H. Richard, K. Ehrenfried, B. G. van der Wall, C. L. Burley, P. Beaumier, K. McAlister, and K. Pengel. Recording and Evaluation Methods of PIV Investigations on a Helicopter Rotor Model. In *Experiments in Fluids 36*, pages 146–156. Springer Verlag, 2004.

[21] W.J.M Rankine. *Manual of Applied Mechanics*. C. Griffen Co., London, 1858.

[22] M. Roth. *Automatic Extraction of Vortex Core Lines and other Line Type Features for Scientific Visualization*. PhD thesis, ETH, 2000.

[23] G. Scheuermann. *Topological Vector Field Visualization with Clifford Algebra*. PhD thesis, University of Kaiserslautern, Germany, 1999.

[24] G. Scheuermann, H. Krüger, M. Menzel, and A. Rockwood. Visualizing Nonlinear Vector Field Topology. *IEEE Transactions on Visualization and Computer Graphics*, 4(2):109–116, 1998.

[25] D. Sujudi and R. Haimes. Identification of Swirling Flow in 3-D Vector Fields. In *AIAA Paper 95-1715, 12th AIAA CFD Conference*, San Diego, 1995.

[26] X. Tricoche. *Vector and Tensor Field Topology Simplification, Tracking, and Visualization*. PhD thesis, University of Kaiserslautern, Germany, 2002.

[27] X. Tricoche, G. Scheuermann, and H. Hagen. A Topology Simplification Method for 2D Vector Fields. In D. Ebert, M. Gross, and B. Hamann, editors, *Proceedings of IEEE Visualization 2000*, pages 359–366, Los Alamitos, CA, 2000. IEEE Computer Society Press.

[28] X. Tricoche, G. Scheuermann, and H. Hagen. Tensor Topology Tracking: A Visualization Method for Time-Dependent 2D Symmetric Tensor Fields. In *Eurographics 2001 Proceedings, Computer Graphics Forum 20(3)*, pages 461–470, Saarbrücken, Germany, 2001. The Eurographics Association.

[29] B. G. van der Wall, C. L. Burley, Y. H. Yu, H. Richard, K. Pengel, and P. Beaumier. The HART II Test - Measurement of Helicopter Rotor Wakes. *Aerospace Science and Technology*, 8(4):273–284, 2004.

[30] G.H. Vatistas. New Model for Intense Self-Similar Vortices. *Experiments in Fluids*, 14(4):462–469, 1998.